Quantum transport of planar Josephson junctions with Majorana bound states

B. H. Wu,* S. A. Hassan, X. F. Xu, and C. R. Wang
Department of Applied Physics, Donghua University, 2999 North Renmin Road, Shanghai 201620, China

W. J. Gong
College of Sciences, Northeastern University, NO. 3-11, Wenhua Road, Shenyang 110004, China

J. C. Cao
Key Laboratory of Terahertz Solid-State Technology, Shanghai Institute of Microsystem and Information Technology, Chinese Academy of Sciences, 865 Changning Road, Shanghai 200050, China

(Received 9 March 2020; revised 22 June 2020; accepted 3 August 2020; published 11 August 2020)

We investigate the transport features of a planar Josephson junction which was recently proposed and verified as a host of Majorana bound states (MBSs). With finite phase difference, MBSs can be gapped from the excited states at moderate Zeeman field. A considerable amount of current density develops at the stripe edges due to the presence of the MBSs. More interestingly, we note that in detecting MBSs via scanning tunneling spectroscopy (STM), a conductance minimum is observed at the peak position of the MBS local density of states. We ascribe this discrepancy to the fact that the penetration of the pair potential decays away the superconducting/normal interface. These results are instructive in not only for identifying MBSs in planar Josephson junction via STM measurement, but also for the detection of MBSs in platforms with nonuniform pair potentials.

DOI: 10.1103/PhysRevB.102.085414

I. INTRODUCTION

Majorana bound states (MBSs) [1–3] are exotic quasiparticles in condensed matter. These zero-energy states are free of charge and localized at the edges of topological superconductors. Two spatially separated MBSs can define a fermion mode. This nonlocal nature leads to potential applications in topologically protected quantum computing where features such as teleportation [4] and non-Abelian braiding [5] are possible. However, the realization of MBSs needs superconducting *p*-wave pairing [6] which is extremely rare in nature. At present stage, several strategies have been put forward to circumvent this challenge using either topological or conventional materials. For example, by taking advantage of the experimentally accessible high-quality semiconductor materials, one proposal requires the engineering of the Zeeman field and spin-orbit interaction in proximity-induced *s*-wave superconductors. As a result, conventional materials have been driven into a topological nontrivial state where MBSs reside. Such material systems include one-dimensional magnetic atom chains [7], semiconductor nanowires [8–10], two-dimensional topological insulators [11,12], and the surface of iron-based superconductors [13–16]. In recent studies [17,18], experiment evidences such as the quantized conductance have confirmed the validity of the theoretical proposals.

To go beyond the detection of a single MBS [19], it remains challenging in developing a scalable platform of MBSs network for the purpose of realistic applications. Both high-quality material growth and material parameter tuning are main obstacles. One important progress in overcoming these challenges was the recent proposed planar Josephson junction [20,21]. Experiments have demonstrated the possibility to induce superconductivity in semiconducting two-dimensional electron gas (2DEG) [22,23]. The interplay of the pair potentials in the superconducting leads, the spin-orbit interaction, and the in-plane magnetic field in 2DEG, can give birth to MBSs at the ends of the normal stripe in the junction. One advantage of this scheme is it is compatible with the advanced planar material and device processing technologies. More interestingly, the emergence of MBSs can be steered by tuning the superconducting phase difference via either biased supercurrent or a threaded magnetic flux. This theoretical prediction has recently been tested experimentally and signatures of the existence of MBSs have been reported [24,25]. The main evidence is the phase-dependent zero-bias conductance peak measured by a laterally coupled quantum point contact (QPC). However, this tunneling spectroscopy of a QPC cannot provide the microscopic details such as the spatial profile of the low-energy eigenmodes in the junction.

In identifying the MBSs, the scanning tunneling microscopy (STM) [26] has been an indispensable tool in providing the microscopic details of the quasiparticle. Advanced techniques in STM have enabled the real-space imaging of electronic structures of material surface with picometer resolution [27]. The quantized differential conductance [28,29] and the spin-selective Andreev reflection [30–32] measured in STM are hallmark evidences for the existence of MBSs. The STM measurement is also useful in revealing the localized nature of MBSs [33]. In previous studies, the comparison

*bhwu2010@gmail.com

of the zero-bias conductance mapping and the profile of the local density of states (LDOS) [27,34] has been accepted as a benchmark in identifying its localized nature in real space in either one-dimensional nanowire [7,35] or two-dimensional platforms [12,14,15,36]. It is thus interesting to investigate the STM signatures in a planar Josephson junction in the pursuing MBSs. We note that the STM signal in Josephson junctions has different mechanisms as compared to the normal conductors. For the latter process, the carrier transport composes normal tunneling and the conductance is proportional to the LDOS at the material surface. This picture needs correction in the presence of the superconductivity where the conductance may be dominated by the Andreev reflection [30]. As a result, the STM conductance depends on not only the LDOS but also the pair potential. This becomes more intriguing in the nonuniform pair potential, such as the Josephson junction mentioned above, where the STM mapping is expected to deviate from the LDOS profile. Detailed investigation on the transport features such as the peculiar STM signal and the Josephson current in the planar Josephson junction would thus be desirable in the pursuing of MBSs.

In this paper we numerically investigate the energy spectrum and transport properties of a planar Josephson junction where MBSs might reside. The main results are summarized in the following. (1) The phase difference can be an efficient tool in inducing MBSs. Finite phase difference can lower the required Zeeman field in pursuing MBSs. The material can then be tuned into a topological nontrivial state and the MBS will be gapped from the excited states at moderate Zeeman field. (2) The planar Josephson junction is an effective φ_0 junction where the Josephson current is finite at zero phase difference. Josephson current density at the ends can be significant due to the localized MBSs. (3) As the penetration of the pair potential decays in the center of the junction, the peak position of the MBS LDOS at the center of the stripe end can no longer coincide with the STM conductance peak, though the LDOS of MBS are highly localized. This observation is in sharp contrast to STM of normal materials where the differential conductance normally follows the LDOS profile of the substrate. Our results then indicate that one should take care when analyzing the STM measurements in superconducting substrates with nonuniform pair potentials.

The paper is organized as follows: Sec. II describe the device configuration and the model Hamiltonian. Section III presents our numerical results, including the energy spectrum, the Josephson current, and the STM mapping of the planar Josephson junction. Transport signatures of the MBSs in planar Josephson junctions are discussed. Finally, the main findings are summarized in Sec. IV.

II. MODEL DEVICE AND THEORETICAL FORMALISM

The model system is a planar Josephson junction consisting of a 2DEG with Rashba spin-orbit coupling. The 2DEG acquires superconductivity by proximity contacting with superconductors on the top. A central stripe is left in normal state. The resulting Josephson junction is then supposed to host MBSs at the stripe ends in the presence of an in-plane magnetic field. A schematic plot of the model device is depicted in Fig. 1 where the 2DEG is placed in the xy plane.

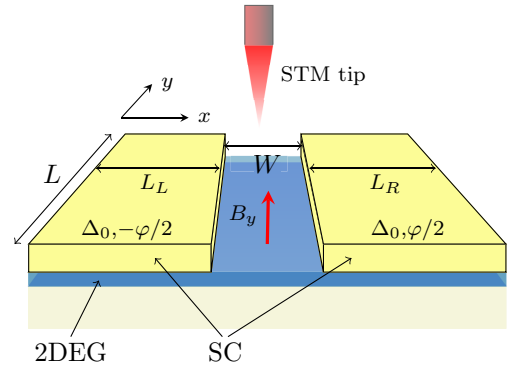

FIG. 1. Schematic plot of the planar Josephson junction. Other than the central stripe, the 2DEG obtains finite pair potential Δ_0 due to the proximity coupling with superconductors. The Rashba spin-orbit interaction, the in-plane magnetic field, and the possibly phase difference across the junction can drive the material into topologically nontrivial with MBSs at the stripe ends. An STM tip can scan the stripe by measuring the differential conductance.

The coordinate origin is assumed at the stripe center. The width and length of the stripe are W and L, respectively. For the sake of simplicity, the pair potentials in the two leads are assumed to have the same magnitude but different phases. The effective Hamiltonian for the normal 2DEG can be written as

$$H_0 = \frac{\boldsymbol{p}^2}{2m} - \alpha^R(p_x\sigma_y - p_y\sigma_x) + E_Z(x)\sigma_y - \mu, \qquad (1)$$

where m is the effective mass, $\boldsymbol{p} = (p_x, p_y)$ is the momentum operator in the xy plane, μ is the chemical potential, and $\sigma_{x,y,z}$ are Pauli matrices in spin space. α^R is the Rashba spin-orbit coupling strength. The Zeeman field $E_Z(x)$ is induced by an external magnetic field B_y along y direction. $E_Z(x)$ is assumed to be confined in the stripe and piecewise constant in the x direction. In the stripe ($|x| < W/2$), $E_y(x) = V_y$. In the superconducting areas ($|x| > W/2$), $E_y(x) = 0$. The proximity-induced pair potential in the 2DEG is accounted for by

$$\Delta(\boldsymbol{r}) = \Delta_0 e^{i\varphi_\alpha}\theta(|x| - W/2), \qquad (2)$$

where Δ_0 is the magnitude and φ_α with $\alpha = L, R$ are the phase in the left (L) and right (R) superconductors, respectively. The phase difference across the junction is given by $\varphi = \varphi_L - \varphi_R$. This phase bias can be introduced by either a supercurrent across the junction or an external threaded magnetic flux. The device can be described by the Bogoliubov–de Gennes Hamiltonian as

$$H_{\mathrm{BdG}} = \begin{pmatrix} H_0 & -i\sigma_y\Delta(\boldsymbol{r}) \\ i\sigma_y\Delta^*(\boldsymbol{r}) & -H_0^* \end{pmatrix}\psi_n(\boldsymbol{r}) = E_n\psi_n(\vec{r}), \qquad (3)$$

where the Nambu spinor $\psi(\boldsymbol{r}) = [u_\uparrow(\boldsymbol{r}), u_\downarrow(\boldsymbol{r}), v_\uparrow(\boldsymbol{r}), v_\downarrow(\boldsymbol{r})]^T$ with $\uparrow$ ($\downarrow$) for spin up (down) and the superscript T for transpose. Due to the particle-hole symmetry, the eigenstates must appear in pairs, i.e., both $[u_\uparrow(\boldsymbol{r}), u_\downarrow(\boldsymbol{r}), v_\uparrow(\boldsymbol{r}), v_\downarrow(\boldsymbol{r})]^T$ and $[-v_\uparrow^*(\boldsymbol{r}), -v_\downarrow^*(\boldsymbol{r}), u_\uparrow^*(\boldsymbol{r}), u_\downarrow^*(\boldsymbol{r})]^T$ are eigenfunctions with eigenenergy E_n and $-E_n$, respectively. For eigenstates with energies below Δ_0, the wave functions are confined in the normal stripe. When the material system is in the topological nontrivial state, MBSs bound states emerge at the stripe ends.

The self-adjoint of the MBSs leads to zero energy of the states. In finding these eigenstates, we first write the Hamiltonian in the real-space tight-binding form and then numerically diagonalize the resulting matrix to solve the eigenproblem. Details on the process are outlined in the Appendix. For the purpose of numerically tractable, we have assumed finite size of the leads. As depicted in Fig. 1, L_L and L_R are, respectively, the length of the left and right superconductor leads. The lengths are much larger than the width of the stripe to avoid finite-size effect in finding the low-energy eigenstates.

In this work we are interested in the transport properties such as the phase biased Josephson current through the junction and the differential conductance when an STM tip is coupled to the stripe surface. Different theoretical formalisms based on Green's function method are applied in revealing these transport features.

For the Josephson current-phase relation, we apply the recursive Matsubara Green's function method [37,38] based on the tight-binding Hamiltonian to evaluate the equilibrium current. Both the current through the junction and the current density can be obtained in the stripe where the current is conserved due to the absence of pairing potential. By including an external perpendicular magnetic field via the Peierls substitution [39], the interference of the supercurrent can be evaluated from our numerical simulation. Details on the formalism are presented in the Appendix.

To obtain the STM mapping, we need to evaluate the differential conductance through the normal STM dip as shown in Fig. 1. The coupling Hamiltonian between the tip and the stripe surface can be given by

$$H_T = \sum_{\boldsymbol{k}} \tilde{\psi}_0(\boldsymbol{k}) \tilde{t}_T \psi(\boldsymbol{r}) + \text{H.c.}, \tag{4}$$

where $\tilde{\psi}_0(\boldsymbol{k})$ represents the quantum state at the tip end with quantum number $\boldsymbol{k}$. $\tilde{t}_T$ is the tunnel coupling between the tip end and the stripe surface at position $\boldsymbol{r}$. We evaluate the differential conductance by making use of the nonequilibrium Green's function as outlined in the Appendix. In the tight-binding model we assume the tip end couples only with one grid. By moving the tip over the stripe surface, a zero-bias STM conductance mapping can be obtained. The mapping results will be compared with the LDOS of MBSs to detect its localized feature at zero energy.

III. NUMERICAL RESULTS AND DISCUSSION

In the following we present numerical results on the transport properties of the planar Josephson junctions as shown in Fig. 1. For better comparison with experiments [24], we have the electron effective mass $m = 0.026\ m_e$ where m_e is the bare electron mass. The spin-orbit coupling strength is fixed at $\alpha^R = 150$ meV Å. We take Δ_0 as the energy unit in the following. The pair potentials in the left and right superconductors are identical with $\Delta_0 = 180\ \mu$eV. The relative phase difference across the junction is φ and the chemical potential $\mu = 1.5\ \Delta_0$ where a pair of MBSs could emerge in our device. With varying μ, the device can be driven into different topological nontrivial phases [40]. The geometry of the two superconductors are $L = 1.6\ \mu$m and $L_L = L_R = 2\ \mu$m as indicated in Fig. 1. The temperature is fixed at $T = 1.0 \times 10^{-3}\Delta_0$ to avoid thermal effect on the transport signature of MBSs. In comparison with experiments, the temperature should be taken into account with realistic values.

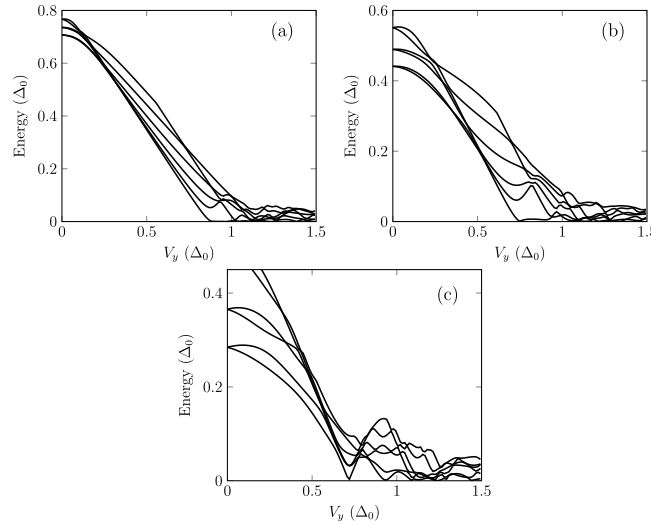

FIG. 2. Lowest six eigenenergies E_n of the planar Josephson junction as functions of the Zeeman field V_y at zero phase difference φ. The stripe widths are (a) $W = 80$ nm, (b) $W = 160$ nm, and (c) $W = 240$ nm, respectively. With increasing V_y, the ground state energy can approach zero, indicating topological phase transition.

A. Eigenenergies and wave functions

A key ingredient in inducing the MBSs in the planar Josephson junction is the high-quality proximity to nearby superconductors. The superconductivity can penetrate into the 2DEG and establish an effective, though weak, uniform pairing potential. When a normal stripe is laterally connected to the left and right superconducting 2DEG, the pairing potential is expected to leak into the normal conductor. The transverse Zeeman field and the spin-orbit interaction at the central stripe can then transform it into an effective one-dimensional topological superconductor where MBSs can reside at the stripe ends. Previous studies [20,21,40] have shown that the phase difference across the junction is a key factor in inducing the MBSs. However, as the leaked pair potential decays drastically with increasing the distance to the interface, the stripe width W is expected to plays a vital role in hosting MBSs.

We now investigate the emergence of MBSs in planar Josephson junctions for different stripe width and phase difference. The width parameters $W = 80$, 160, and 240 nm have been adopted, where $W \ll L_{L/R}$ to reduce the finite size effect of the superconductors. We first investigate situations at zero phase bias, i.e., $\varphi = 0$. The lowest six eigenenergies E_n of the device as functions of the transverse Zeeman field V_y are depicted in Fig. 2. These eigenenergies are obtained by solving the effective BdG Hamiltonian Eq. (3) in the tight-binding form. Due to the particle-hole symmetry, only positive eigenenergies are displayed here. In the absence of Zeeman field ($V_y = 0$), the eigenenergies are pair degenerate due to time-reversal symmetry and the device is in the topological

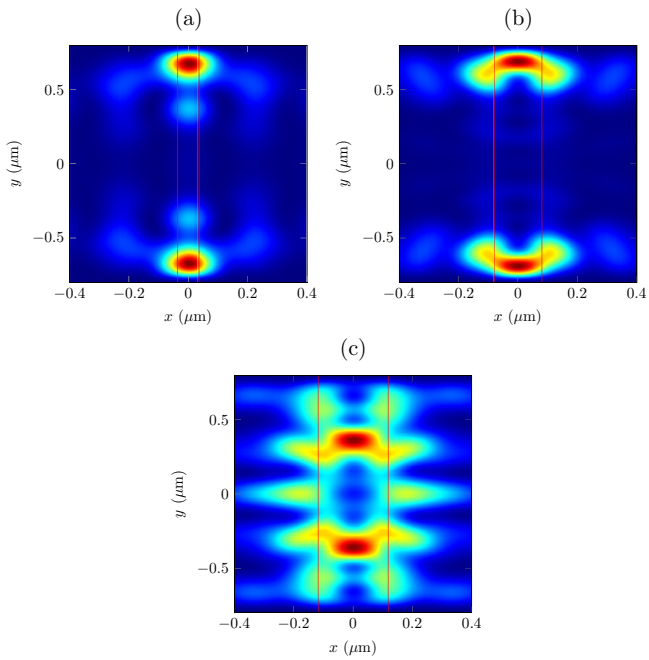

FIG. 3. Contour plots of the probability densities of the ground states with Zeeman field $V_y = 0.9\ \Delta_0$ and $\varphi = 0$. The widths of the stripe are (a) $W = 80$ nm, (b) $W = 160$ nm, and (c) $W = 240$ nm. The other parameters are identical with those in Fig. 2. The interface of the the stripe and the nearby superconductors are indicated by the red lines. The ground state wave function is distorted by increasing the stripe width.

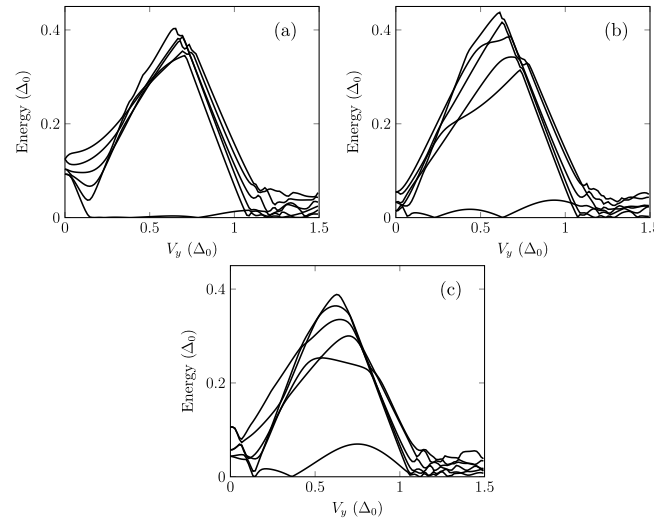

FIG. 4. In the presence of finite phase bias $\varphi = \pi$, the lowest eigenenergies E_n with regards to the Zeeman field V_y for the three devices in Fig. 2. Again we have the stripe width (a) $W = 80$ nm, (b) $W = 160$ nm, and (c) $W = 240$ nm. The phase bias shows its advantages in driving the material system into topological states at very Zeeman field and the significant gap between the ground state and the excited states.

trivial regime. With increasing V_y, the degeneracy is broken and the eigenvalues display a similar trend. They all decrease until the lowest one approaches zero, indicating a topological phase transition. The corresponding critical field of V_y is less than Δ_0 and the exact value is width dependent. After this phase transition, the behavior of the ground state with lowest eigenenergy is closely related to the stripe width W. For narrow stripe [$W = 80$ nm, Fig. 2(a)], the lowest energy stays close to zero for a finite range of V_y. A finite gap between the ground state to the excited states with higher energies can be identified. This gap remains robust until the excited states approach zero at larger Zeeman field where the states mix with each other. The parameter range of V_y defined by the phase transition and the state mixing is vital for potential applications of MBSs. To demonstrate the appearance of the MBSs, we plot the wave function magnitudes $|\psi(x, y)|^2$ of the ground state at $V_y = 0.9\ \Delta_0$ in Fig. 3(a). Two sharp peaks of the wave function magnitude are localized at the stripe ends, a clear evidence of the MBSs. With larger stripe width [$W = 160$ nm, Fig. 2(b)], the ground state energy after phase transition deviates from zero with increasing V_y. Again, a clear gap can be observed between the ground state and the other excited states. In Fig. 3(b) we present the corresponding wave function magnitudes $|\psi(x, y)|^2$ of the ground state at $V_y = 0.9\ \Delta_0$. Although the wave function is localized at the stripe ends, the spatial distribution is broadened and the shape is distorted as compared to Fig. 3(a). Obviously each $|\psi(x, y)|^2$ peak at the stripe end develops two arms extending into the nearby superconductors. With further increasing the stripe width $W = 240$ nm, the ground state energy in Fig. 2(c) displays a pronounced oscillation with increasing V_y after the phase transition. As a result, the ground state mixes with the exited states and no clear gap can be identified from the figure. In Fig. 3(c) the contour plot of the ground state wave function magnitude $|\psi(x, y)|^2$ at $V_y = 0.9\Delta_0$ is presented for comparison. Although the wave functions are mostly localized in stripe, two clear arms penetrating into the superconductors can be observed. More interestingly, the wave function peaks are no longer residing at the stripe ends. They appear somewhere in the central section of the stripe. This feature suggests that the ground state is no longer topologically nontrivial due to the mixing with the excited states. These observations prove that the stripe width W should be carefully designed in future applications of the MBSs in planar Josephson junctions.

Previous studies [20,21] have shown that finite phase difference φ across the junction can significantly change the topological state. In Figs. 4 and 5 we present the eigenenergies and the corresponding ground state wave function distribution for the same parameters in Fig. 2, except the phase bias $\varphi = \pi$. We adopt a symmetric phase bias with $-\varphi_L = \varphi_R = \varphi/2$. For all the stripe width parameters in Fig. 4, the critical field of V_y for the topological phase transition is significantly reduced at $\varphi = \pi$. For example, for the small width $W = 80$ nm, the ground state energy at $\varphi = \pi$ approaches zero for V_y less than $0.2\ \Delta_0$ as shown in Fig. 4(a), while this parameter is greater than $0.7\ \Delta_0$ for $\varphi = 0$ as indicated in Fig. 2(a). This merit lowers the required magnitude of the external Zeeman field and benefits future applications with a stable pairing potential in the device. Another advantage of the finite phase difference is that after the phase transition, the ground state remains close to zero and the energies of the excited states are markedly different in a wide parameter range of V_y.

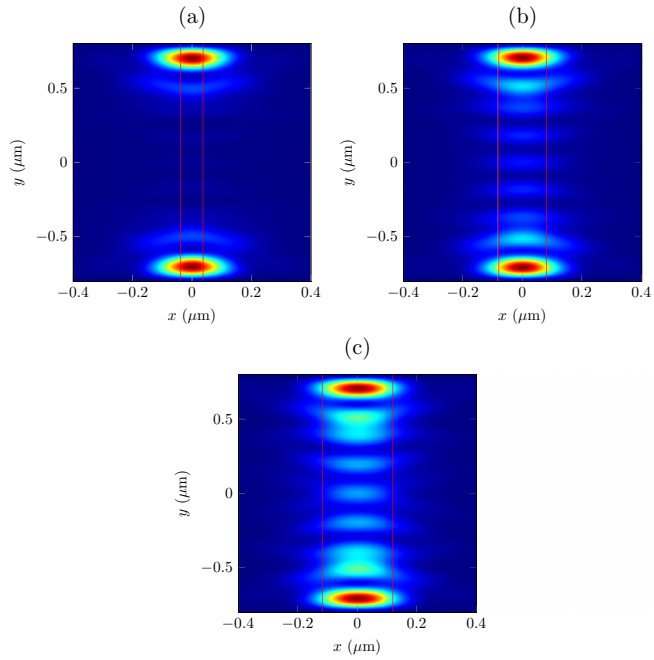

FIG. 5. Contour plots of the probability densities of the ground states with Zeeman field $V_y = 0.9\ \Delta_0$ and $\varphi = \pi$. The widths of the stripe are (a) $W = 80$ nm, (b) $W = 160$ nm, and (c) $W = 240$ nm. The other parameters are identical with those in Fig. 3. The interface of the the stripe and the nearby superconductors are indicated by the red lines.

Different from Fig. 2, one can identify from Fig. 4(a) that the maximum gap between the states can be more than $0.35\Delta_0$ for $W = 80$ nm. The large differences in energy scale are crucial for identifying and manipulating MBSs in potential applications where the MBS wave function would be less affected by the hybridization with the excited states. These results prove that the phase bias φ can be an effective tool in not only tuning the topological phase transition, but also setting up a robust gap between the zero-energy ground state and the excited states. The numerical results also indicate that the ground state energy can be affected by the stripe width. After the topological phase transition, the ground state energy remains close to zero for narrow stripe. With increasing the stripe width, the ground state displays an enhanced oscillatory variation. Our results show that the finite phase cannot only open a considerable gap, but also leave the MBS wave function profile less distorted by the stripe width. This should be in contrast to situations with vanishing phase bias. In Fig. 5 we have presented the contour plot of the ground state wave functions for different W with phase bias $\varphi = \pi$ and fixed $V_y = 0.7\ \Delta_0$. For all three devices, the MBS wave functions are localized at the stripe ends. In particular, for the largest stripe width [$W = 240$ nm, Fig. 5(c)], though one can find that ripple structures in places between the stripe ends become more prominent, two sharp peaks each at the stripe ends remains intact, in distinct contrast to situations with $\varphi = 0$ [Fig. 3(c)]. These observations show that the phase bias could be a beneficial factor in pursuing MBSs. We now investigate the evolution of the eigenspectrum as a function of the phase bias. The numerical results are presented in

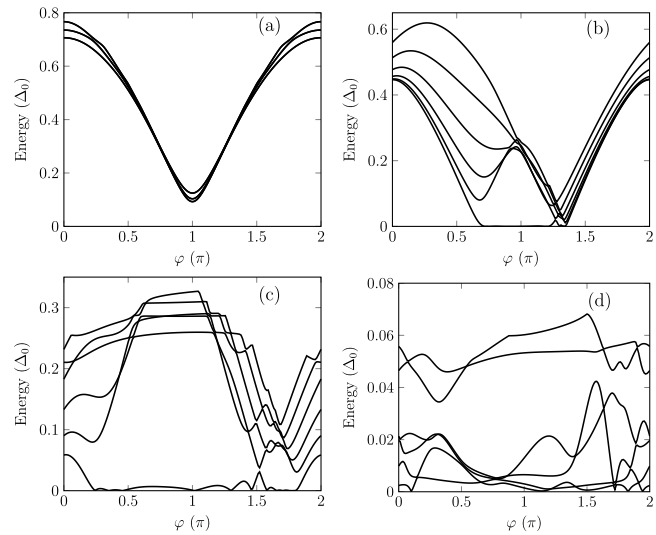

FIG. 6. The evolution of the lowest eigenenergies as functions of the phase bias φ with different Zeeman field: (a) $V_y = 0$, (b) $V_y = 0.4\ \Delta_0$, (c) $V_y = 0.8\ \Delta_0$, and (d) $V_y = 1.2\Delta_0$. The stripe width $W = 80$ nm. By tuning φ, the ground state can approach zero at moderate Zeeman field V_y.

Fig. 6. In the numerical simulation we have fixed the stripe width $W = 80$ nm and several parameters of the transverse Zeeman field V_y are taken. Figure 6(a) displays the results in the absence of Zeeman field. As expected, the energies spectrum are symmetric with respect to $\varphi = \pi$. The lowest energies cannot become zero, indicating the absence of topological phase transition without Zeeman field. With finite V_y as shown in Figs. 4(b)–4(d), the eigenenergies can approach zero at finite phase bias, indicating the phase transition and emergence of MBSs. For $V_y = 0.4\ \Delta_0$ [Fig. 6(b)], the ground state energy remains at zero in the finite parameter range of φ. A clear gap can be identified between the ground state and the other excited states. In these situations, stable MBSs can be expected. With increased field $V_y = 0.8\ \Delta_0$ [Fig. 6(c)], the parameter range for phase transition is enhanced. The excited states are slightly lowered while the energy gap remains clear in the spectrum. Moreover, the ground state energy displays an oscillatory behavior with varying phase bias. This oscillation becomes more prominent for a larger Zeeman field as shown in the figure. With the largest Zeeman field $V_y = 1.2\ \Delta_0$ [Fig. 6(d)], the excited states are lowered in the entire phase range and hybridization between the lowest eigenstates can be inferred from the figure. In that way the gap between the MBS and higher excited states becomes vague. This situation is detrimental to applications of MBSs which should be robust against environment disturbance. These results indicate that a careful design of the planar Josephson junction with MBSs needs optimization of parameters such as the stripe width, phase bias, and the Zeeman field.

B. Anomalous Josephson current and interference pattern

Another observation from Fig. 6 is that the spectrum becomes asymmetric with finite Zeeman field. This can be ascribed to the broken time-reversal symmetry by the external

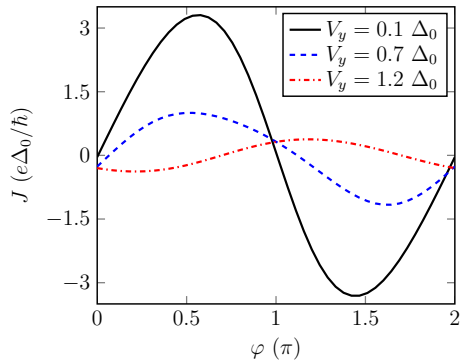

FIG. 7. The Josephson current-phase relation in a planar Josephson junction. The other parameters are identical with those in Fig. 6 except the Zeeman fields are $V_y = 0.1\ \Delta_0$ (solid black line), $0.7\ \Delta_0$ (dash-dotted red line), and $1.2\ \Delta_0$ (dashed blue line). In the presence of a Zeeman field, the Josephson current J at zero phase bias can be nonzero.

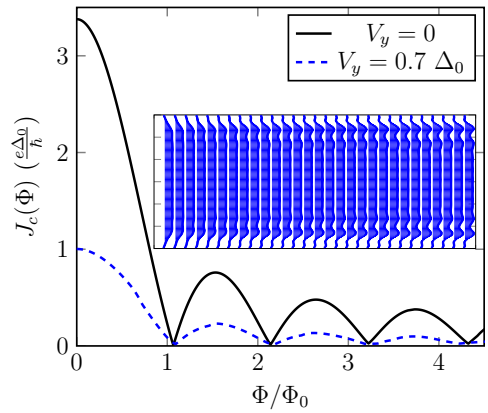

FIG. 8. With an external magnetic field $B_\perp$ perpendicular to the junction, the interference pattern of the critical Josephson current $J_c(\Phi)$ is displayed as a function of the external magnetic flux $\Phi = B_\perp S$ where S is the stripe area. The stripe width $W = 80$ nm. Different in-plane Zeeman fields V_y are investigated. In the presence of an in-plane Zeeman field V_y, the critical current is reduced. The inset shows the supercurrent density in the stripe calculated at $V_y = 0.7\ \Delta_0$ and $\varphi = \pi$. One can clearly identify the contribution of the MBSs at the stripe ends to the current density.

field. As the ground state of the Josephson junction is offset, one would expect it to be turned into a so-called φ_0 junction where the Josephson current is finite at zero phase bias. This observation is verified in our numerical results. We evaluate the equilibrium Josephson current by the Matsubara Green's function method [37,38] which is outlined in the Appendix. Figure 7 depicts the Josephson current-phase relation for a different Zeeman field. The stripe width is fixed at 80 nm. By tuning the Zeeman field V_y, an anomalous Josephson current-phase relation can be demonstrated. The maximum Josephson current which appears at $0 < \varphi < \pi$ at $V_y = 0.1\ \Delta_0$ has been shifted to $\pi < \varphi < 2\pi$ at $V_y = 1.2\ \Delta_0$. Another observation is that the Josephson current at $\varphi = 0$ now takes finite values at nonzero V_y. Regarding the recent experiments [24] in realizing the planar Josephson junction with MBSs, it would be interesting to detect this φ_0 junction [41] where the Josephson current bias is used to producing MBSs.

It is known that the Josephson current can be periodically modulated by an external magnetic field [42]. The interference pattern of the critical Josephson current as a function of the magnetic flux can reveal the current density information. For the planar Josephson junction, not only the bulk state in the stripe, but also the localized MBSs at the stripe ends, can carrier Josephson current and contribute to the interference pattern. Figure 8 depicts our numerical results of the interference pattern of the critical Josephson current in either the normal ($V_y = 0$) or the nontrivial ($V_y = 0.7\ \Delta_0$) state. The external magnetic field perpendicular to the 2DEG is described by the Peierls substitution [39] and the formalism for evaluating the Josephson current is given in the Appendix. The critical Josephson current J_c is obtained by sweeping the phase bias φ across the junction at a given flux Φ as [38]

$$J_c = \max\{J_\Phi(\varphi)\}. \tag{5}$$

We estimate the flux $\Phi = B_\perp S$, where $B_\perp$ is the magnetic field perpendicular to the junction plane and $S = WL$ is the junction area. For normal junction with $V_y = 0$, the evolution of the critical supercurrent with regards to the flux is a classical Fraunhofer pattern as shown in Fig. 8. The curve is smooth and the magnitude of the side lobes decreases with increasing flux Φ. The local minimum of the critical Josephson current is very close to zero at flux Φ being multiples of the flux quantum $\Phi_0 = h/2e$ due to destructive interference. This interference pattern indicates that the supercurrent takes uniform distribution in the bulk according to the Dynes-Fulton analysis [43]. With finite V_y, the variation of phase bias φ can bring the junction into topological nontrivial situations. In particular, the MBSs at the stripe ends are expected to change the current distribution by carrying supercurrent at the edges. In Fig. 8 the numerical results for $V_y = 0.7\ \Delta_0$ is also presented. According to previous analysis, MBSs are expected in such situations. Compared with the situations with $V_y = 0$, the interference pattern does not show drastic changes as compared with results in the absence of V_y. However, one can detect that the magnitudes of each side lobe are lowered and the local minimum positions display slight deviation from the previous curve. The decreasing of the side lobes can be ascribed to the Zeeman splitting which is adverse to the supercurrent. While the deviation provides clues for the change of the supercurrent density distribution in the presence of MBSs.

For a better view on the role of MBSs in carrying supercurrent, we present an example of the supercurrent density distribution in the junction in the inset of Fig. 8. The supercurrent density is obtained by evaluating the bond supercurrent between the nearest-neighbor sites in a tight-binding model as described in the Appendix. The Zeeman field $V_y = 0.7\ \Delta_0$. the phase bias across the junction is fixed at $\varphi = \pi/4$. At the left interface of the stripe, the incident supercurrent is almost uniformly distributed in the bulk. With the current flowing to the right, the density at the strip edges becomes gradually prominent, indicating the increasing role of localized MBSs in carrying the supercurrent. However, the supercurrent density at the edges cannot overwhelm the uniform distribution in the bulk. As a result, no significant change has been detected

in the interference pattern. We note that the local minimum positions display slight change, indicating the deviation of the current distribution.

C. Local density of states and differential conductance

In a recent experiment [24] the MBSs in the planar junction are detected by a quantum point contact (QPC). It would be desirable to provide microscopic details on the exotic quasiparticle. A scanning tunneling microscopy (STM) measurement could be an indispensable tool for that purpose. The working principle is that the differential conductance of STM tips would be proportional to the LDOS at the material surface. One would expect the localized LDOS of MBSs can provide zero-bias differential conductance peak in the mapping of MBSs. In particular, the MBS-assisted resonant Andreev reflection would lead to quantized conductance, a hallmark of the emergence of MBSs. This characteristic transport feature has been detected in various platforms which may host MBSs. The platforms include nanowires with induced superconductivity and superconducting thin films with vortices. A recent study has recorded the quantized conductance at the end of a nanowire where the MBS resides. Moreover, the STM mapping has provided evidence for the existence of MBSs at the surface of topological insulators or iron-based superconductors. However, a factor which has largely been overlooked is that the LDOS profile cannot be directly associated with the differential conductance in the presence of superconductivity. The differential conductance is related to not only the LDOS but also the pair potential profile in the Andreev reflection processes. This is not a crucial issue in detecting MBS in nanowires where the wire acquires uniform pair potential due to proximity effect. However, it becomes intricate in situations with a nonuniform pair potential profile such as the vortex at superconducting surfaces and the planar Josephson junctions. In the following we present our results on the comparison of the LDOS and the corresponding differential conductance. Our results show that as the penetration of the pair potential decays in the center of the junction, the localized MBSs can no longer be identified by a conductance peak, though the LDOS of MBS are highly localized. These observations are crucial in detecting MBSs with nonuniform pair potential.

The LDOS $D(E)$ can be obtained by the imaginary part of the retarded Green's function. The LDOS at position $\boldsymbol{r} = (x, y)$ in the junction can be obtained by

$$D(E;\boldsymbol{r}) = -\frac{1}{\pi}\sum_{\sigma=\uparrow,\downarrow} \mathrm{Im}G^r(E;\boldsymbol{r};\boldsymbol{r})_{\sigma\sigma}, \tag{6}$$

where G^r is the retarded Green's function of device as $G^r(\omega) = (E - H_{\mathrm{BdG}} + i\eta)^{-1}$ with η being a positive infinitesimal. In Fig. 9 we present the zero-energy LDOS $D(E = 0)$ in the normal stripe. Due to symmetry, results are depicted in areas with $y < 0$. The junction width $w = 80$ or 240 nm, representing the narrow and wide junction. The magnetic field $V_y = 0.7\ \Delta_0$. The phase difference φ was used to tune the junction into topological trivial ($\phi = 0$) or nontrivial ($\phi = \pi$) states. For the narrow junction ($W = 80$ nm), the LDOS in the stripe is shown in Figs. 9(a) and 9(b) for $\varphi = 0$ and $\varphi = \pi$, respectively. For the trivial situation [Fig. 9(a)], a substantial LDOS at the junction bulk area is observed. This

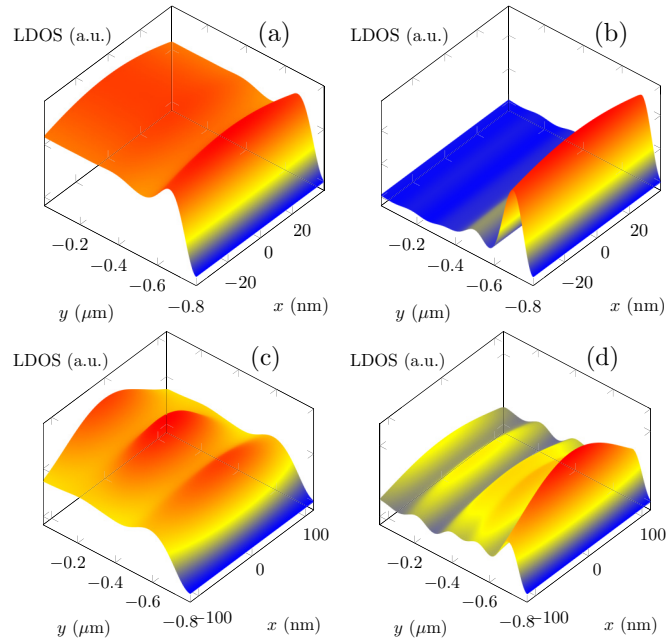

FIG. 9. The zero-energy LDOS $D(E = 0)$ in half of the stripes ($y < 0$) at $V_y = 0.7\ \Delta_0$ with different stripe width W and phase bias φ. (a) $W = 80$ nm, $\varphi = 0$, (b) $W = 80$ nm, $\varphi = \pi$, (c) $W = 240$ nm, $\varphi = 0$, and (d) $W = 240$ nm, $\varphi = \pi$. For $\varphi = 0$, the device in the topological trivial state while for $\varphi = \pi$, MBSs at the stripe edges appear where the peak of the LDOS is fixed at the edge center ($x = 0$).

should be in contrast to the nontrivial case in Fig. 9(b) where a MBS channel at the edge becomes significant while it becomes negligible at the bulk. Another observation is that the local maximum of LDOS is at $x = 0$. It would be slightly reduced away from $x = 0$, forming a MBS edge channel in the stripe. In the wide junction limit, for $W = 240$ nm, the results shown in Figs. 9(c) and 9(d) display similar behavior of the LDOS. The main difference is that the MBSs in the wide junction becomes more localized along the stripe edge. A clear peak of LDOS at the junction edge can be identified along x direction. The peak position is fixed at $x = 0$. For the sake of comparison, we present in Fig. 10 the corresponding zero-bias differential conductance profiles for $\varphi = 0$ or π in the narrow ($W = 80$ nm) or wide ($W = 240$ nm) junctions. The zero-bias differential conductance $G(\boldsymbol{r}) = dI/dV|_{V=0}$ is measured by assuming an STM tip is posited at $\boldsymbol{r}$. The coupling between the tip and the stripe is characterized by the strength $\Gamma = 500\ \Delta_0$. Symmetry allows us to present results only in areas with $y < 0$. For the wide junctions, only results in $x < 0$ and $y < 0$ are presented due to symmetry reasons. From previous results of the eigenspectrum, the junction is in the trivial (nontrivial) states for $\varphi = 0$ (π). For the trivial situation, results shown in Fig. 10(a) and 10(c) are obtained for $W = 80$ nm and $W = 240$ nm, respectively. The dI/dV profiles are significant at both the junction edge and central area. In particular, the conductance remains significant at the junction edge for the wide junction ($W = 240$ nm) as shown in Fig. 10(c). This conductance profile changes drastically in the topological nontrivial situations as shown in Figs. 10(b)

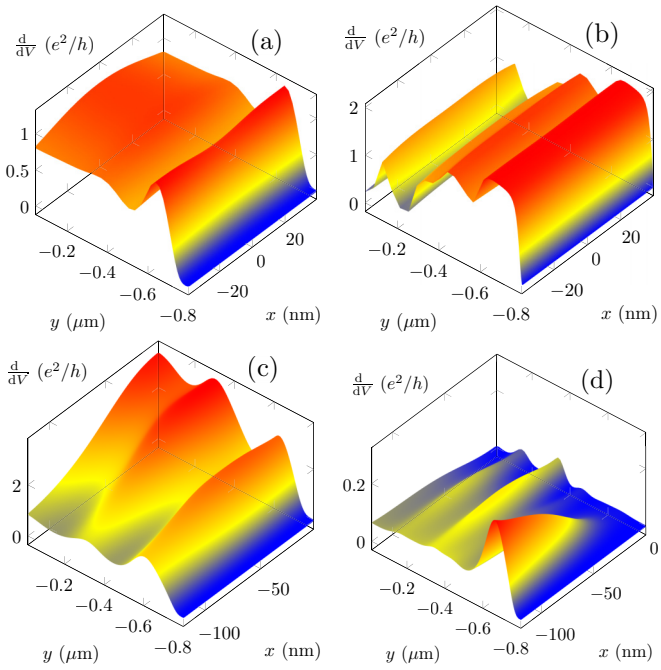

FIG. 10. Zero-bias differential conductance measured by the STM tip for the same parameters as in Fig. 9. The stripe width and phase bias are given by (a) $W = 80$ nm, $\varphi = 0$, (b) $W = 80$ nm, $\varphi = \pi$, (c) $W = 240$ nm, $\varphi = 0$, and (d) $W = 240$ nm, $\varphi = \pi$. For the narrow stipe $W = 80$ nm [(a) and (b)], we present the conductance mapping at half of the stripe ($y < 0$), while for the wide stripe with $W = 240$ nm [(c) and (d)], only conductance mapping at $x < 0$ and $y < 0$ is displayed for the sake of symmetry. Note the conductance at the edge center for $\varphi = \pi$ takes local minimum where the LDOS has a peak value due to the MBSs.

and 10(d). Figure 10(b) displays dI/dV profile for narrow junctions with $W = 80$ nm where the conductance takes its maximum along its edge while the conductance at the central area of the junction has been significantly reduced. These observations are in qualitative agreement with the LDOS profile as shown in Fig. 9. However, the positions of the conductance peak in Fig. 10(b) and LDOS profile in Fig. 9(b) no longer coincide at the edge center where the MBS is expected to reside. With increasing the junction width, the conductance at the edge center will be suppressed. This can be more pronounce in wider junctions. In Fig. 10(d) the junction has $W = 240$ nm and MBSs. Obviously the conductance is suppressed at the edge center ($x = 0$) as in drastic contrast to the LDOS results shown in Fig. 9(d). Along the edge, the conductance increases as the tip moves away from the center. We ascribe this peculiar feature to the fact that the resonant Andreev reflection processes [30] due to MBSs is sensitive to the pair potential. As the pair potential in the normal stripe is due to the leaking from the nearby superconductor leads. This penetration decays as the distance from leads increases. This becomes most prominent in wide stripes as the pair potential at the stripe center can be comparable to the thermal energies of electrons. It is known that the Andreev reflection process which dominant the tunneling transport via MBSs is sensitive to the variation of the pair potential [42]. When thermal electrons are injected, the probability for Andreev

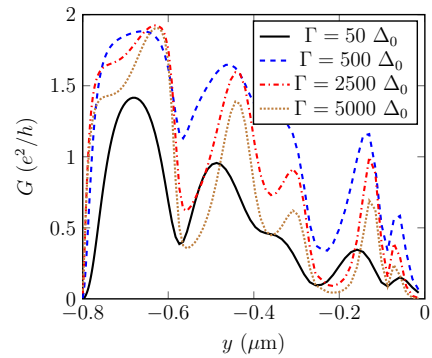

FIG. 11. Zero-bias differential conductance $G = dI/dV|_{V=0}$ measured along the y axis at $x = 0$ with different coupling Γ between the STM tip and the surface. The maximum conductance near the edge approaches the quantized value of $2e^2/h$ with increasing Γ. Only results for the lower panel ($y < 0$) of the device are presented.

processes would then be reduced around $x = 0$. As a result, the differential conductance profile displays a local minimum at the edge center of the stripe where the MBSs are expected to reside. Although these observations are obtained for the planar Josephson junction, we note that the conclusion applies to situations where the nonuniform pair potential exists. For example, in the recent platform with vortices [12,14–16], the MBSs are expected to reside in the vortex center where the pair potential is zero. Therefore, a direct comparison between the STM conductance mapping and the LDOS need careful analysis in identifying MBSs.

Finally, we show that although the conductance at edge center takes local minimum, its magnitude can be enhanced by increasing the coupling strength Γ between the tip and the stripe. In Fig. 11 we present the conductance along y axis at $x = 0$ for different Γ. With increasing Γ from 50 Δ_0 to 5000 Δ_0, the conductance peak value which locates near the edge can approach the quantized value $2e^2/h$. This feature is in accordance to previous studies [44,45] where quantized conductance of MBSs $2e^2/h$ is expected in the large coupling strength and lower temperature limit due to the resonant Andreev reflection. By tuning the coupling strength, the evolution of the conductance can serve as a probe in identifying the MBSs.

IV. CONCLUSION

In conclusion, we have investigated the transport features of the planar Josephson junction where the MBSs may reside. Our results show that the superconducting phase across the junction can modify the band structure and drive the device into topological nontrivial situations. In the presence of finite phase difference, MBSs can be gapped from the excited states at moderate Zeeman field. As the external Zeeman field breaks the time-reversal symmetry, the planar Josephson junction can be an effective φ_0 junction. A significant portion of the supercurrent density is carried by the localized MBSs. As a result, the supercurrent interference pattern can deviate from a conventional Fraunhofer curve in normal states. More interestingly, we note that in detecting MBSs in the stripe via STM conductance, the LDOS peak of MBSs does not coincide

with the conductance maximum as the penetration of the pair potential decays away the interface between superconductor and normal stripe. Therefore, it may be inadequate to characterize the MBSs via STM measurement in nonuniform pair potentials. Other tools [12,31] such as the spin-resolved STM or the characteristic noise features might provide alternative means in identifying the MBSs. We leave these studies for future works ahead. In addition, we note that the observations in this study are relevant in identifying MBSs in not only planar Josephson junction, but also for other platforms such as vortices where nonuniform pair potentials exist.

ACKNOWLEDGMENTS

This work was supported by the National Science Foundation of China (Grant. No. 61975029), Natural Science Foundation of Shanghai (Grants No. 16ZR1447800 and No. 19JC1416802), the Fundamental Research Funds for the Central Universities (Grant No. N170506007), and the Liaoning BaiQianWan Talents Program (Grant No. 201892126).

APPENDIX

In this Appendix we present some details of our theoretical method in evaluating the transport properties of the planar Josephson junction.

1. Tight-binding Hamiltonian

As mentioned in the main text, our calculations are made in real space. The physical quantities can be discritized on grid points in the xy plane. For a uniform grid with lattice spacing a, the Hamiltonian of Eq. (3) can be written in the tight-binding form as

$$\mathcal{H} = \sum_{ij}\{\psi_{ij}^{\dagger}H_{ij;ij}\psi_{ij} + \psi_{ij}^{\dagger}H_{ij;i+1,j}\psi_{i+1,j} + \psi_{ij}^{\dagger}H_{i,j+1}\psi_{i,j+1}\} + \text{H.c.}, \tag{A1}$$

where the grid index i and j are along x and y direction, respectively. The matrix elements are given as

$$H_{ij} = \begin{pmatrix} \frac{2\hbar^2}{ma^2}-\mu & -iE_{ij}^{Z} & 0 & -\Delta_{ij} \\ iE^{Z}(ij) & \frac{2\hbar^2}{ma^2}-\mu & \Delta_{ij} & 0 \\ 0 & \Delta_{ij}^{*} & -\frac{2\hbar^2}{ma^2}+\mu & -iE_{ij}^{Z} \\ -\Delta_{ij}^{*} & 0 & iE_{ij}^{Z} & -\frac{2\hbar^2}{ma^2}+\mu \end{pmatrix}, \tag{A2}$$

$$H_{i+1,j} = \begin{pmatrix} -\frac{\hbar^2}{2ma^2} & \alpha_{ij}^{R}\frac{1}{2a} & 0 & 0 \\ -\alpha_{ij}^{R}\frac{1}{2a} & -\frac{\hbar^2}{2ma^2} & 0 & 0 \\ 0 & 0 & \frac{\hbar^2}{2ma^2} & -\alpha_{ij}^{R}\frac{1}{2a} \\ 0 & 0 & \alpha_{ij}^{R}\frac{1}{2a} & \frac{\hbar^2}{2ma^2} \end{pmatrix}, \tag{A3}$$

$$H_{i,j+1} = \begin{pmatrix} -\frac{\hbar^2}{2ma^2} & i\alpha_{ij}^{R}\frac{1}{2a} & 0 & 0 \\ i\alpha_{ij}^{R}\frac{1}{2a} & -\frac{\hbar^2}{2ma^2} & 0 & 0 \\ 0 & 0 & \frac{\hbar^2}{2ma^2} & i\alpha_{ij}^{R}\frac{1}{2a} \\ 0 & 0 & i\alpha_{ij}^{R}\frac{1}{2a} & \frac{\hbar^2}{2ma^2} \end{pmatrix}. \tag{A4}$$

A direct diagonalization would be expensive as the dimension of the Hamiltonian would be huge. This can be seen from the fact that the typical values of the stripe width is much smaller than the device length. As a result a large number of grids are needed. To reduce the computation cost, one can make use of the nonuniform grid since the MBSs are mainly localized at the stripe ends. In addition, high performance routines such as the ARPACK [46] are efficient in finding the lowest eigenstates.

2. Josephson current

Equilibrium Josephson current can be driven through the junction by a phase difference φ. The Josephson current can be given by

$$J(\varphi) = -\frac{ie}{\hbar}\sum_{j}\langle\psi_{ij}^{\dagger}H_{i+1,j}\psi_{i+1,j} - \psi_{i+1,j}^{\dagger}H_{i+1,j}^{\dagger}\psi_{ij}\rangle, \tag{A5}$$

where the expectation $\langle\cdots\rangle$ stands for thermal average. The expression gives the current from the ith layer to the $i+1$th layer in the stripe. When a perpendicular magnetic field is applied in z direction, interference of the Josephson current takes place. To obtain the interference pattern, we take into account the magnetic field by replacing the hopping matrix elements by the Peierls substitution [39]. For example, the matrix elements of $H_{i+1,j}$ which represents the electron hopping between site (i, j) and $(i+1, j)$ should multiply a factor $\exp(-ieB_{\perp}a^2 j/\hbar)$, where $B_{\perp}$ is the perpendicular magnetic field.

With the help of the Matsubara Green's function, the Josephson current can be given by [37,38]

$$J(\varphi) = -\frac{ie}{\beta\hbar}\sum_{\omega_n}\text{Tr}[\mathcal{H}_{i+1;i}G_{i;i+1}(\omega_n) - G_{i+1;i}(\omega_n)\mathcal{H}_{i;i+1}], \tag{A6}$$

where the trace (Tr) is taken over the spin space and the j site index. $\mathcal{H}_{i;i+1}$ is the block Hamiltonian coupling the ith and $(i+1)$th layer. $\beta = 1/k_BT$ with k_B the Boltzmann constant, T is the temperature. $G_{i;i+1}(\omega_n)$ is the block matrix of the Nambu Green's function with the Matsubara frequency $\omega_n = \pi k_BT(2n+1)$ as

$$G(\omega_n) = [i\omega_n - \mathcal{H} - \Sigma_L(\omega_n) - \Sigma_R(\omega_n)]^{-1}, \tag{A7}$$

where $\Sigma_{L/R}$ represents the self-energy function of the semi-infinite L and R superconducting leads. These self-energies can be found by conventional recursive algorithms [47] and the block matrix of Green's function $G_{i;i+1}(\omega_n)$ can be obtained effectively via the recursive Green's function algorithm [39]. In numerical simulation, i can be any layer in the stripe. As the pair potential in the stripe is zero, the current is conserved in the stripe. We have numerically verified this statement to check the accuracy of the numerical results.

3. Differential conductance of STM tip

In the calculation we have fixed the chemical potential of the 2DEG at zero. The voltage is applied to the normal STM tip. We evaluate the differential conductance of the STM tip via the nonequilibrium Green's function method [48].

In the wide-band limit, the coupling between the tip and stripe surface at position $\boldsymbol{r}$ in Eq. (4) leads to the retarded self-energy

$$\Sigma_{\boldsymbol{r}}^{R}(\varepsilon) = -i\Gamma, \tag{A8}$$

where $\Gamma = \pi \sum_{\boldsymbol{k}} |\tilde{t}_T|^2 \delta(\varepsilon - \varepsilon_{\boldsymbol{k}})$ is an energy-independent coupling constant. Here $\varepsilon_{\boldsymbol{k}}$ represents the energy of the state $\tilde{\psi}_0(\boldsymbol{k})$ in the tip. The corresponding advanced self-energy is given by $\Sigma_{\boldsymbol{r}}^{A}(\varepsilon) = [\Sigma_{\boldsymbol{r}}^{R}(\varepsilon)]^{\dagger}$.

In the tight-binding form we assume the tip couples to a single site and the self-energy can be written as $\Sigma_{ij}^{R} = \Sigma_{\boldsymbol{r}=\boldsymbol{r}_{ij}}^{R}$, where $\boldsymbol{r}_{ij}$ is the grid coordinates. Based on the tight-binding Hamiltonian, the retarded Green's function can be obtained by Dyson equation as

$$G^{R}(\varepsilon) = [\varepsilon - \mathcal{H} - \Sigma_{ij}^{R}]^{-1}. \tag{A9}$$

The advanced Green's function is then given by $G^{A}(\varepsilon) = G^{R}(\varepsilon)$.

The lesser Green's function which represents the particle occupation can be evaluated by the Keldysh equation as

$$G^{<}(\varepsilon) = G^{R}(\varepsilon)\Sigma^{<}(\varepsilon)G^{A}(\varepsilon), \tag{A10}$$

where the lesser self-energy $\Sigma^{<}(\varepsilon)$ is given by

$$\Sigma^{<}(\varepsilon) = 2i\Gamma\sigma_0 \otimes \begin{pmatrix} f(\varepsilon - eV) & 0 \\ 0 & f(\varepsilon + eV) \end{pmatrix}. \tag{A11}$$

Here $f(\varepsilon)$ is the Fermi-Dirac distribution function with V the voltage in the tip.

With the self-energies and Green's functions at the coupling site (i, j), we may express the current through the tip as

$$I = \frac{e}{\hbar} \int d\varepsilon \mathrm{ReTr}\left\{\hat{\boldsymbol{\sigma}}\left[G_{ij}^{<}(\varepsilon)\Sigma_{ij}^{A}(\varepsilon) + G_{ij}^{R}(\varepsilon)\Sigma_{ij}^{<}(\varepsilon)\right]\right\}. \tag{A12}$$

Here Tr stands for the trace of the matrix. $\hat{\boldsymbol{\sigma}} = \mathrm{diag}[1, 1, -1, -1]$ accounts for the different charge of electron and hole. From Eq. (A12) the difference conductance can be evaluated.

[1] J. Alicea, Rep. Prog. Phys. **75**, 076501 (2012).
[2] C. Beenakker, Annu. Rev. Condens. Matter Phys. **4**, 113 (2013).
[3] S. R. Elliott and M. Franz, Rev. Mod. Phys. **87**, 137 (2015).
[4] L. Fu, Phys. Rev. Lett. **104**, 056402 (2010).
[5] C. Nayak, S. H. Simon, A. Stern, M. Freedman, and S. Das Sarma, Rev. Mod. Phys. **80**, 1083 (2008).
[6] A. Kitaev, Ann. Phys. **321**, 2 (2006).
[7] S. Nadj-Perge, I. K. Drozdov, J. Li, H. Chen, S. Jeon, J. Seo, A. H. MacDonald, B. A. Bernevig, and A. Yazdani, Science **346**, 602 (2014).
[8] J. D. Sau, R. M. Lutchyn, S. Tewari, and S. Das Sarma, Phys. Rev. Lett. **104**, 040502 (2010).
[9] R. M. Lutchyn, J. D. Sau, and S. Das Sarma, Phys. Rev. Lett. **105**, 077001 (2010).
[10] Y. Oreg, G. Refael, and F. von Oppen, Phys. Rev. Lett. **105**, 177002 (2010).
[11] L. Fu and C. L. Kane, Phys. Rev. Lett. **100**, 096407 (2008).
[12] H.-H. Sun, K.-W. Zhang, L.-H. Hu, C. Li, G.-Y. Wang, H.-Y. Ma, Z.-A. Xu, C.-L. Gao, D.-D. Guan, Y.-Y. Li, C. Liu, D. Qian, Y. Zhou, L. Fu, S.-C. Li, F.-C. Zhang, and J.-F. Jia, Phys. Rev. Lett. **116**, 257003 (2016).
[13] G. Xu, B. Lian, P. Tang, X.-L. Qi, and S.-C. Zhang, Phys. Rev. Lett. **117**, 047001 (2016).
[14] D. Wang, L. Kong, P. Fan, H. Chen, S. Zhu, W. Liu, L. Cao, Y. Sun, S. Du, J. Schneeloch, R. Zhong, G. Gu, L. Fu, H. Ding, and H.-J. Gao, Science **362**, 333 (2018).
[15] C. Chen, Q. Liu, T. Z. Zhang, D. Li, P. P. Shen, X. L. Dong, Z.-X. Zhao, T. Zhang, and D. L. Feng, Chin. Phys. Lett. **36**, 057403 (2019).
[16] T. Machida, Y. Sun, S. Pyon, S. Takeda, Y. Kohsaka, T. Hanaguri, T. Sasagawa, and T. Tamegai, Nat. Mater. **18**, 811 (2019).
[17] V. Mourik, K. Zuo, S. M. Frolov, S. R. Plissard, E. P. A. M. Bakkers, and L. P. Kouwenhoven, Science **336**, 1003 (2012).
[18] H. Zhang, C.-X. Liu, S. Gazibegovic, D. Xu, J. A. Logan, G. Wang, N. van Loo, J. D. S. Bommer, M. W. A. de Moor, D. Car, R. L. M. O. het Veld, P. J. van Veldhoven, S. Koelling, M. A. Verheijen, M. Pendharkar, D. J. Pennachio, B. Shojaei, J. S. Lee, C. J. Palmstrøm, E. P. A. M. Bakkers, S. D. Sarma, and L. P. Kouwenhoven, Nature (London) **556**, 74 (2018).
[19] H. Zhang, D. E. Liu, M. Wimmer, and L. P. Kouwenhoven, Nat. Commun. **10**, 5128 (2019).
[20] M. Hell, M. Leijnse, and K. Flensberg, Phys. Rev. Lett. **118**, 107701 (2017).
[21] F. Pientka, A. Keselman, E. Berg, A. Yacoby, A. Stern, and B. I. Halperin, Phys. Rev. X **7**, 021032 (2017).
[22] Z. Wan, A. Kazakov, M. J. Manfra, L. N. Pfeiffer, K. W. West, and L. P. Rokhinson, Nat. Commun. **6**, 7426 (2015).
[23] M. Kjaergaard, F. Nichele, H. J. Suominen, M. P. Nowak, M. Wimmer, A. R. Akhmerov, J. A. Folk, K. Flensberg, J. Shabani, C. J. Palmstrøm, and C. M. Marcus, Nat. Commun. **7**, 12841 (2016).
[24] A. Fornieri, A. M. Whiticar, F. Setiawan, E. Portolés, A. C. C. Drachmann, A. Keselman, S. Gronin, C. Thomas, T. Wang, R. Kallaher, G. C. Gardner, E. Berg, M. J. Manfra, A. Stern, C. M. Marcus, and F. Nichele, Nature (London) **569**, 89 (2019).
[25] H. Ren, F. Pientka, S. Hart, A. T. Pierce, M. Kosowsky, L. Lunczer, R. Schlereth, B. Scharf, E. M. Hankiewicz, L. W. Molenkamp, B. I. Halperin, and A. Yacoby, Nature (London) **569**, 93 (2019).
[26] G. Binnig, K. H. Frank, H. Fuchs, N. Garcia, B. Reihl, H. Rohrer, F. Salvan, and A. R. Williams, Phys. Rev. Lett. **55**, 991 (1985).
[27] W. A. Hofer, A. S. Foster, and A. L. Shluger, Rev. Mod. Phys. **75**, 1287 (2003).
[28] K. T. Law, P. A. Lee, and T. K. Ng, Phys. Rev. Lett. **103**, 237001 (2009).
[29] K. Flensberg, Phys. Rev. B **82**, 180516(R) (2010).

[30] J. J. He, T. K. Ng, P. A. Lee, and K. T. Law, Phys. Rev. Lett. **112**, 037001 (2014).
[31] B. H. Wu, W. Yi, J. C. Cao, and G.-C. Guo, Phys. Rev. B **90**, 205435 (2014).
[32] L.-H. Hu, C. Li, D.-H. Xu, Y. Zhou, and F.-C. Zhang, Phys. Rev. B **94**, 224501 (2016).
[33] D. Chevallier and J. Klinovaja, Phys. Rev. B **94**, 035417 (2016).
[34] S. Lounis, arXiv:1404.0961 .
[35] M. Ruby, F. Pientka, Y. Peng, F. von Oppen, B. W. Heinrich, and K. J. Franke, Phys. Rev. Lett. **115**, 197204 (2015).
[36] T. Kawakami and X. Hu, Phys. Rev. Lett. **115**, 177001 (2015).
[37] A. Furusaki, Phys. B: Condens. Matter **203**, 214 (1994).
[38] B. H. Wu, W. J. Gong, X. F. Xu, C. R. Wang, and J. C. Cao, J. Phys.: Condens. Matter **31**, 285301 (2019).
[39] M. Wimmer, Ph.D. thesis, Univ. Regensburg, Regensburg, 2008.
[40] J. Liu, Y. Wu, Q.-F. Sun, and X. C. Xie, Phys. Rev. B **100**, 235131 (2019).
[41] D. B. Szombati, S. Nadj-Perge, D. Car, S. R. Plissard, E. P. A. M. Bakkers, and L. P. Kouwenhoven, Nat. Phys. **12**, 568 (2016).
[42] M. Tinkham, *Introduction to Superconductivity* (Dover, Mineola, NY, 2004).
[43] R. C. Dynes and T. A. Fulton, Phys. Rev. B **3**, 3015 (1971).
[44] C.-X. Liu, J. D. Sau, T. D. Stanescu, and S. Das Sarma, Phys. Rev. B **96**, 075161 (2017).
[45] S. Zhu, L. Kong, L. Cao, H. Chen, M. Papaj, S. Du, Y. Xing, W. Liu, D. Wang, C. Shen, F. Yang, J. Schneeloch, R. Zhong, G. Gu, L. Fu, Y.-Y. Zhang, H. Ding, and H.-J. Gao, Science **367**, 189 (2020).
[46] https://www.caam.rice.edu/software/ARPACK/.
[47] M. P. L. Sancho, J. M. L. Sancho, and J. Rubio, J. Phys. F **15**, 851 (1985).
[48] H. Haug and A.-P. Jauho, *Quantum Kinetics in Transport and Optics of Semiconductors* (Springer, Berlin, 2008).